INSTRUMENTATION

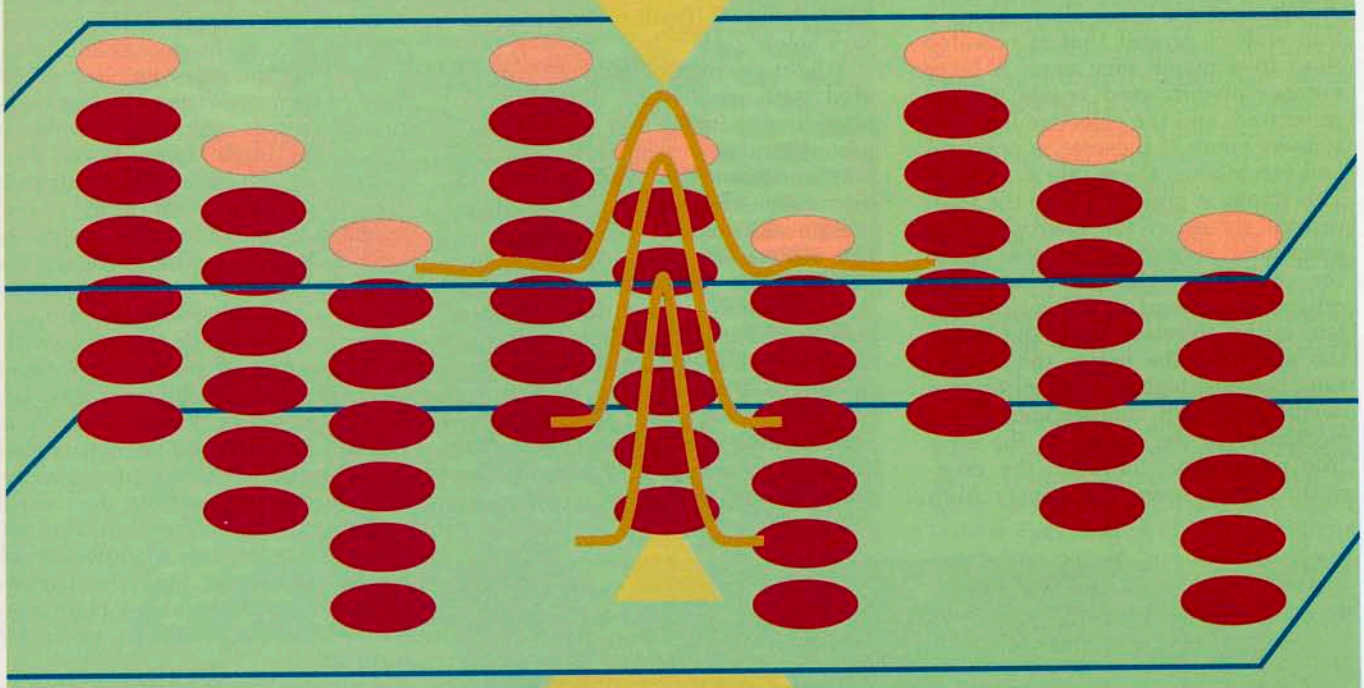

Atomic-Scale Imaging of Materials by *Z*-Contrast Scanning Transmission Electron Microscopy

S. J. Pennycook
Solid State Division
Oak Ridge National Laboratory
Oak Ridge, TN 37831-6030

Materials science is a rapidly expanding field that is capturing the interest of increasing numbers of chemists, physicists, and engineers. Striving to develop new or improved materials now goes hand in hand with obtaining a deeper understanding of fundamental scientific phenomena.

There is no better example of this trend than the recently discovered high-T_c superconducting materials. Because their coherence lengths are only a few atomic spacings, the properties of the material's grain boundary or an interface depend critically on the structure and chemistry of the material on the atomic scale. These properties may differ significantly from those of the bulk material a few lattice spacings farther away. Besides having obvious practical applications, determining the properties of these regions is an excellent, and probably the best, way to improve our fundamental understanding of the material's properties.

The problem is that these critical regions are inaccessible to direct study. Buried inside the material and just a few atomic spacings across, they contribute little to bulk techniques for the analysis of structure or chemistry. X-ray and neutron diffraction, for example, can be used with a high degree of accuracy to determine the average structure, but the properties of many real materials are not controlled by the average structure alone.

When high-T_c materials were first discovered, determination of the basic structure of the unit cell was made within a matter of weeks. Several years later, however, we still have only a sketchy outline of the structure and properties of those grain boundaries and interfaces that control the critical current capacity of a thin film or the characteristics of a superconducting switch.

The technique described in this article is one that I believe opens up such materials problems to fundamental study. It *can* determine the atomic structure and composition within a coherence length of a grain boundary or tunnel junction. *Z*-contrast scanning transmission electron microscopy (STEM) is a completely new approach to high-resolution imaging. Its key advantage is that a material's atomic structure and composition are immediately indicated by the form of the image. Interpretation can be made directly, without the need for any preconceived ideas for interface structure, and thus unanticipated structures are immediately apparent from the image.

Conventional high-resolution electron microscopy

The conventional approach to imaging a crystal lattice is a coherent

0003-2700/92/0364-263A/$02.50/0

phase contrast technique, best thought of as an attempt to reconstruct the object from its diffracted beams (*1*, *2*). As indicated schematically in Figure 1a, a highly collimated electron beam illuminates a thin slab of crystal that is oriented close to a major zone axis. A large number of diffracted beams will be generated, and the objective lens collects as many of these as is practical and recombines them into an image. This image is projected onto the fluorescent screen of the microscope by additional magnifying lenses. As in the case of a light microscope, the critical component in the optical system is the objective lens. The larger the aperture, the better the resolution, because higher angle diffracted beams represent smaller spatial periodicities in the object. In the electron microscope, however, the magnetic lenses have inherently high spherical aberrations (typically 1 mm). These aberrations severely restrict the maximum usable aperture, and even though the electron wavelength at 200 kV is only 0.025 Å, it is difficult to resolve spacings below 2 Å.

A light microscope is usually operated with incoherent illumination, providing an image that can be interpreted straightforwardly in terms of amplitude contrast. With an electron microscope, we are trying to image individual atomic columns; most of the scattered amplitude passes through the objective aperture so that incoherent illumination would give very little image contrast in the conventional arrangement. However, the phase of the electron wave function can be rotated significantly, even several times in crystals a few hundred angstroms in thickness. The conventional approach to imaging has therefore been to employ highly coherent illumination and to form an image based on phase contrast.

Phase changes accumulated by the electron wave function as it travels through the sample will appear at the exit face of the crystal and be encoded into the emerging set of diffracted beams. With a perfect imaging system, it would be possible to recombine the diffracted beams so as to create a phase contrast image in which intensity changes corresponded to phase changes within the crystal. But we see immediately how difficulties of interpretation arise. Whether the phase changes are converted to positive or negative amplitude depends on the phase rotation introduced by the objective lens; this in turn depends on the exact focus setting. Atomic columns can reverse from bright to dark contrast as we alter the focus. To add to the complications, this behavior occurs at different focus settings for different diffracted beams so that the various periodicities in the object can image with different, perhaps reversed, contrast.

A similar complicated behavior occurs as the sample thickness increases. Phase changes along atomic columns can exceed π and again introduce a contrast reversal. A whole set of possible images results for any given object, depending on defocus and sample thickness, as shown in Figure 2a for Si viewed along the ⟨110⟩ direction. The situation is even worse at interfaces, where the image involves interference between diffracted beams from the two perfect crystals on either side and therefore cannot be deduced from the behavior of the two perfect crystals far away from the interface.

Except in very special cases, it is not possible to deduce the object from the image. It is, however, possible to calculate the various images corresponding to a certain model structure, and in so doing to identify the best conditions for imaging. But pretuning the microscope conditions in this way will limit the sensitivity of the image to effects not originally anticipated.

Direct imaging at atomic resolution

What is required to solve materials problems is a technique that can image the structures actually present at an interface, independent of any preconceived ideas concerning probable interfacial arrangements. We need the electron equivalent of incoherent light microscopy. Such a technique is

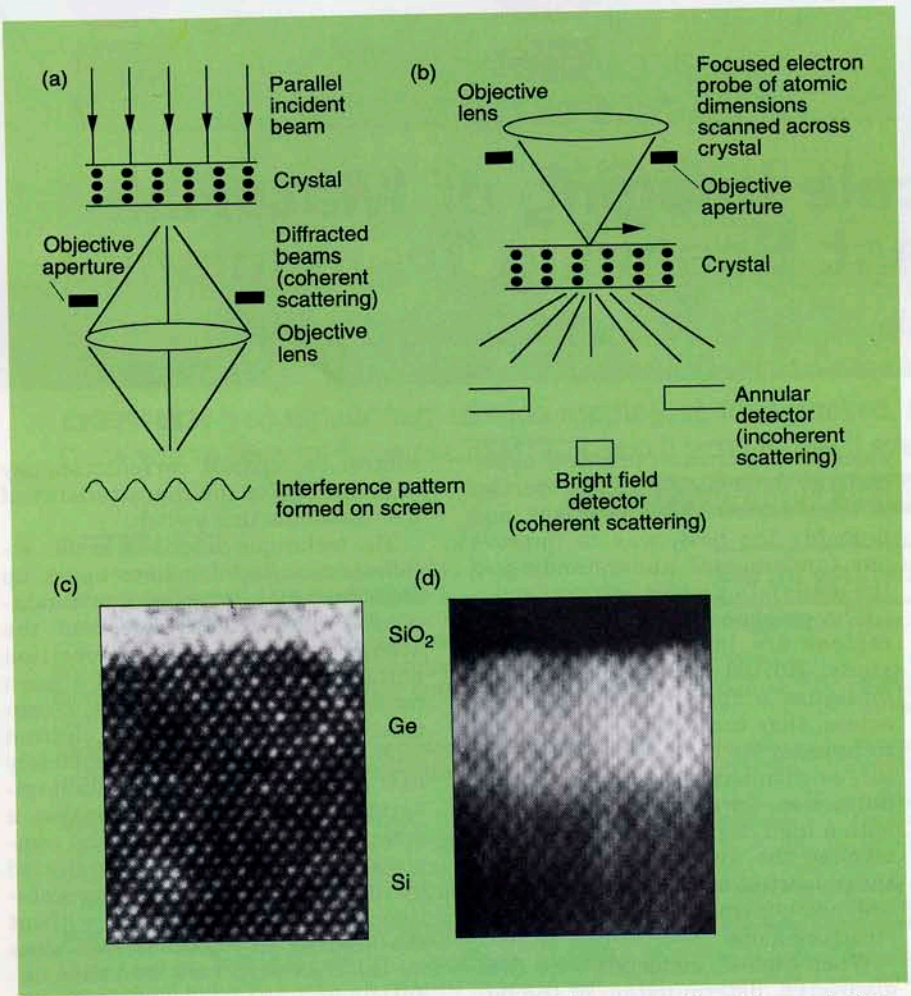

Figure 1. Schematic showing image formation in (a) a conventional transmission electron microscope as a reconstruction from the diffracted beams (coherent imaging) and (b) a scanning transmission electron microscope with an annular detector to provide a map of the scattering power on the atomic scale (incoherent imaging).

Corresponding images from a SiO_2/Ge/Si structure are shown in (c) and (d).

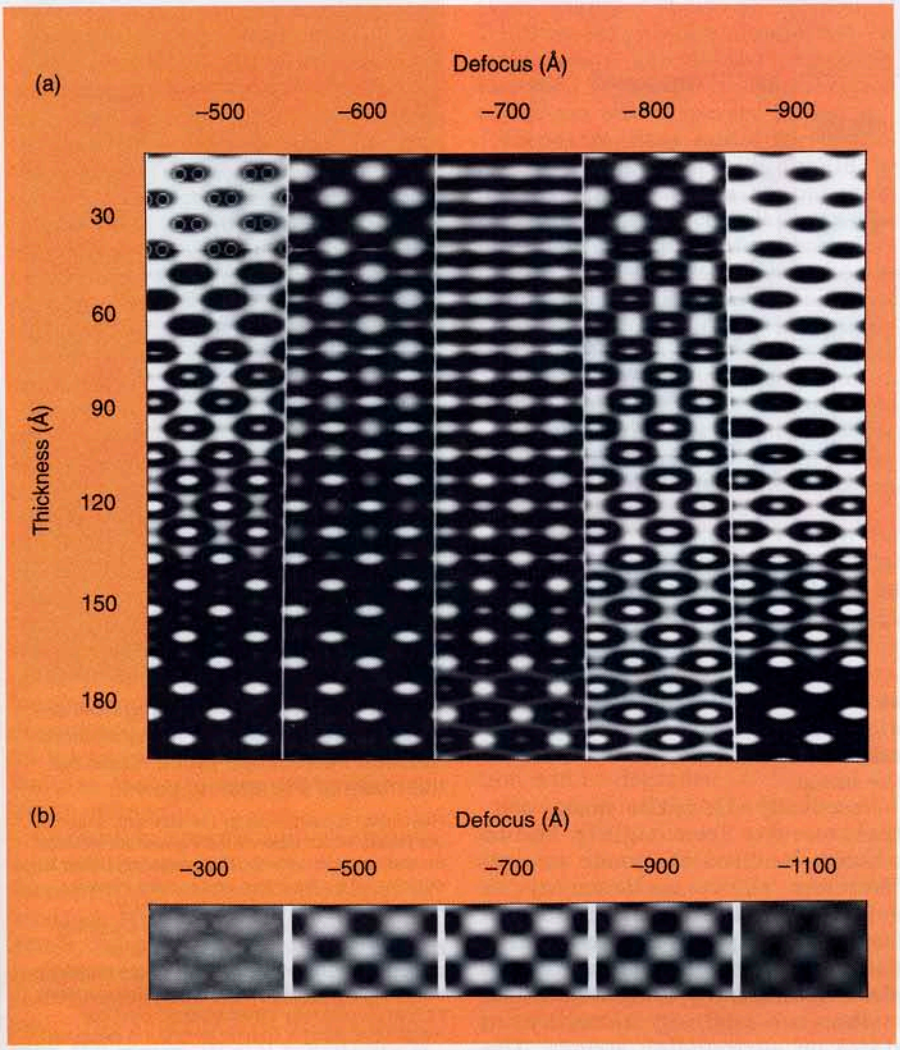

Figure 2. Simulated images from Si viewed along the ⟨110⟩ direction.

(a) Montage of simulated phase contrast images shows a direct correspondence between the projected atom sites (circles) and the image. Contrast reversals occur with increased objective lens defocus or sample thickness. (b) Simulated defocus sequence for *Z*-contrast imaging. With increasing sample thickness the image increases in intensity but retains its general form; atomic columns are always seen bright.

Z-contrast STEM, indicated schematically in Figure 1b. The objective lens is now used to form an electron probe focused to atomic dimensions, which is then scanned across the surface of the thin crystal (*2–4*). Electrons scattered through large angles are collected by an annular detector and used to map out an image as the probe scans the sample.

This image does indeed show incoherent characteristics and atomic resolution (*5*). Because of the effect of thermal vibrations, high-angle Bragg diffracted beams are replaced by thermal diffuse scattering (*6*). This scattering is generated incoherently by each atom, and the resulting image shows the incoherent characteristics familiar from incoherent light microscopy and everyday optical instruments, such as the camera. No contrast reversals occur either with objective lens defocus (Figure 2b) or with increasing sample thickness; a focused image always shows the same form.

The direct correspondence between the object and the image means we can think of the image as a map of the scattering power of the object, with the resolution of the probe. For a sufficiently small probe, individual columns will be imaged with a brightness dependent on their high-angle scattering power. This scattering power shows nearly the Z^2 dependence of unscreened Rutherford scattering, Z being the atomic number. Strong compositional sensitivity is therefore built into the image—hence the term *Z*-contrast imaging.

Figures 1c and 1d compare phase- and *Z*-contrast images of a thin Ge epitaxial layer on a Si substrate covered by amorphous SiO_2. Si and Ge are isostructural and indistinguishable in the phase contrast interference pattern. The *Z*-contrast image represents a column-by-column map of the composition, which clearly changes abruptly from Ge to Si within a single unit cell. It is also instructive to compare the two images of the Ge–SiO_2 interface. The *Z*-contrast image of amorphous SiO_2 is uniform and dark, so that the first columns of the Ge layer are clearly visible, but a coherent image of an amorphous phase shows a characteristic speckle pattern that interferes with and obscures the image from the first Ge layer.

We see how the *Z*-contrast technique provides a clear and unique form of image. If we know a crystal projection, it is relatively easy to imagine the form of the image based on the distribution of columns, their scattering power, and the size of the scanning probe. More importantly, it is also possible to use the location and brightness of image features to determine the likely structure and composition near an interface. In effect, we are able for the first time to look inside materials and see how they are put together on the atomic scale.

Filtering of quantum states. This capability seems all the more remarkable when we consider that the probe itself must have undergone multiple elastic scattering events similar to those responsible for the changing form of the coherent image. However, the *Z*-contrast image appears immune to such effects; it loses contrast gradually with increasing sample thickness but retains the same form.

It is revealing to investigate at a somewhat more fundamental level how the probe propagates through the crystal. If we examine the stationary quantum states for the fast electron inside the crystal, it becomes clear how such characteristics arise. At or near a zone axis, the electron motion can be considered fast along the crystal axis but slow in the transverse plane. Interaction with the periodic crystal potential is correspondingly weak along the axis but strong in the transverse plane, so that the stationary quantum states take on a cylindrical symmetry that is continuous along the axial direction but shows the periodicity of the crystal in the transverse plane.

The transverse nature of such Bloch states can be thought of in a manner entirely analagous to the de-

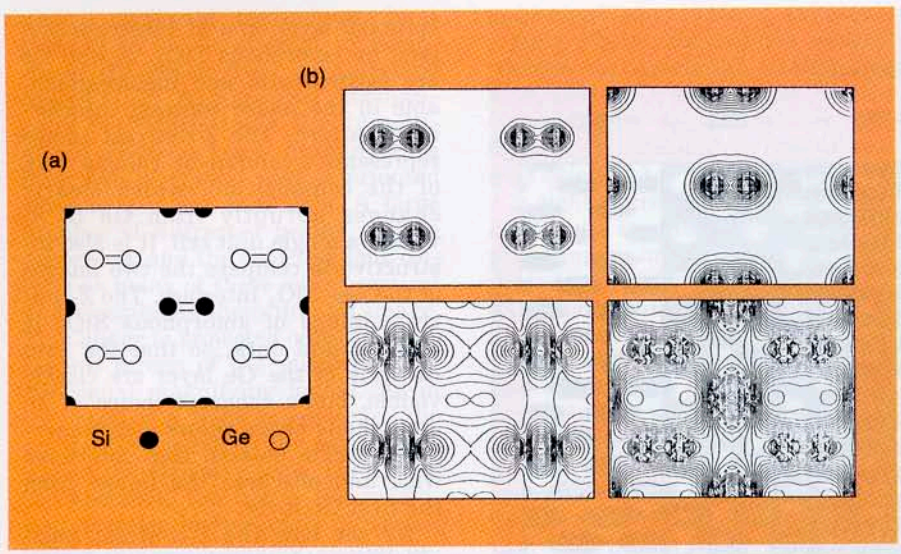

Figure 3. (a) Schematic of a $(Si_2Ge_2)_n$ superlattice viewed along the ⟨110⟩ direction and (b) some associated Bloch states for a 100-kV fast electron.

Only localized s-type states (upper states) are effective in *Z*-contrast imaging.

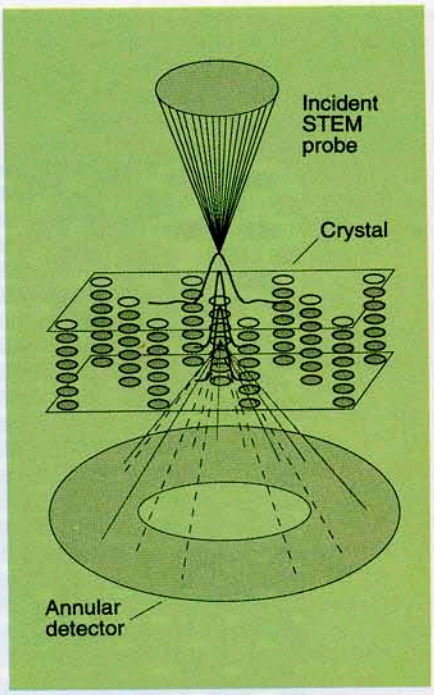

Figure 4. Schematic showing how a finely focused scanning transmission electron microscope probe maps out the material's scattering power.

Resolution is controlled by the size and shape of the probe, which determines the current incident on each atomic column. The scattering power is determined by the integrated s-state intensity along the column (weakly dependent on composition) and by the high-angle scattering cross section (strong Z^2 dependence on composition). Note that the high-angle scattering is a relatively small fraction of the total scattering so that current may travel several hundred Angstroms along a column before it is depleted.

scription of molecular bonding in solid-state chemistry. Individual atomic columns are associated with a set of atomic or molecular orbitals. Figure 3a shows a schematic projection along the ⟨110⟩ direction of a $(Si_2Ge_2)_n$ superlattice; Figure 3b shows some of the Bloch states for a 100-kV electron incident along the same direction of the superlattice (*7*). In this projection, the structure appears as "dumbbells" or closely spaced pairs of identical strings. Each dumbbell has associated localized molecular orbitals (top portion of Figure 3b) comprising bonding and antibonding combinations of individual s-states. At the bottom of Figure 3b are two less localized states: One is centered primarily over the Ge dumbbells (left), and the other represents a hybridization between states on both Si and Ge dumbbells (right). Each Bloch state propagates along the column with a slightly different wave vector; beating between these states is the origin of the depth-dependent interference effects seen in the conventional phase contrast image.

Now consider the case of *Z*-contrast imaging. Scattering through high angles only occurs very close to the atomic sites. The tightly bound s-type states peak strongly in this region and, equally important, they are relatively insensitive to the exact incident beam angle. They are therefore excited in phase by all the incident angles contained in the coherent STEM probe, whereas less localized states are not. The action of the high-angle detector can therefore be seen as a very effective Bloch state filter, a quantum filter preventing less localized states from contributing to the image.

Practically the entire image contrast results from tightly bound s-states localized at atomic strings. Therefore, there can be no strong depth-dependent interference effects, which explains how the form of the image can be insensitive to sample thickness. In addition, these s-states are relatively insensitive to states on surrounding strings. The s-state orbitals in Figure 3b feel only their own dumbbells and contribute to the image just as they would in pure Si or Ge. Therefore, even at interfaces, *Z*-contrast images can be interpreted on a column-by-column basis. This is not true of the less localized states, which is why phase contrast images of interfaces must be calculated explicitly.

An atomic resolution map of the scattering power. We therefore arrive at the simple picture of the imaging process shown in Figure 4. As the probe scans the array of atomic columns, we map out their scattering power with the resolution of the probe. If the probe is sufficiently fine, we will resolve the columns individually and unambiguously.

The relative brightness will reflect their relative scattering power, given by the s-state intensity integrated along the column weighted by the high-angle cross sections. The s-state intensities themselves are only weakly dependent on column composition, which is why the conventional image in Figure 1, for example, cannot distinguish Si from Ge. The *Z*-contrast image is dominated by the nearly Z^2 dependence of the high-angle scattering power, corresponding to an almost fourfold increase from Si to Ge.

To first order, therefore, we have an unambiguous representation of both the position and the relative composition of atomic columns. We can go back from the image to the object and interpret the images intuitively with no a priori assumptions on interface structure and no pretuning of the microscope conditions. Usually we have a good idea of the structures on either side of the interface, and images from these regions can be used to calibrate the intensity scale.

Finally, because only s-states are involved, we can perform image simulations quite simply by calculating the scattering power of the various columns and convoluting it with the probe intensity profile. In this way, the interpretation can be fine-tuned

without restrictions on sensitivity.

Image detail finer than the probe size. The ability to deduce the object from the image is *not* limited to features that are clearly resolved by the probe. The image is controlled by the s-states that are localized spatially on a much finer scale than the incident probe. The probe resolution is simply a definition of when two objects image as two separate peaks; moving the objects closer together will result in a single image feature, but it will be elongated as in the Si dumbbell in Figure 2.

Thus the shapes of image features are also predictable and interpretable intuitively, and information can be extracted from the image at a scale well below the probe size. Figure 5 is an experimental image from Si⟨110⟩ that clearly shows the anticipated elongation of the image features. In the case of InP, however, the scattering power of the two columns comprising the dumbbell is no longer equal. The heavy In string dominates, and the image appears as an array of roughly circular image features that are now centered over the In string (*5*).

Careful interpretation of shapes and relative positions of image features provides excellent sensitivity to interface structure, allowing, for example, monolayer height (1.4 Å) interface steps to be imaged in GaAs/GaInP quantum well structures (*8*) and Si/Ge superlattices. In the latter case, the compositional sensitivity is sufficiently high that new ordered phases have been seen at the interfaces, providing new insight into the atomistic processes occurring during growth (*9*).

Microcrystalline materials. The high-angle annular detector is also of great value with materials whose grain size is too small to allow individual crystallites to be aligned with the electron beam. Supported metal catalysts are an excellent example; in fact, it was to improve the visibility of such clusters that the high-angle detector was originally introduced. These catalysts generally comprise heavy metals on light supports, and *Z*-contrast images reveal the particles with strong contrast, which is particularly valuable as their size approaches the resolution limit of conventional bright field imaging techniques (*10–12*). In addition, because diffraction contrast effects are suppressed, particles can be reliably distinguished from small diffracting regions of the support material. Such characteristics are of great value for determining particle size distributions. Figure 6 shows an example of 7–10-Å Pt clusters supported on γ-alumina, a material that previously has been shown by H chemisorption to contain well-dispersed Pt.

Experimental considerations. A few practical details should be mentioned. To obtain an optimum probe size, the objective lens must be designed specifically for probe formation, because both it and the objective aperture are on the opposite side of the sample from the conventional imaging situation (see Figure 1). To obtain sufficient current in such a probe, a high-brightness field emission source is mandatory; to avoid contamination buildup under the probe, there must be a clean UHV environment.

The same attention should be given to sample preparation as is necessary for conventional high-resolution imaging. It is particularly important to minimize any surface contamination or amorphous layers resulting from ion milling; otherwise, the probe will broaden before it reaches the crystal and the resolution will be degraded.

Keep in mind that the resolution of current STEM display and recording systems is significantly inferior to the information density available with a photographic plate; one generally needs to work at a magnification two or three times higher than that of a conventional transmission electron microscope. However, when STEM is used, the screen brightness remains constant as the magnification is raised.

All images shown here were obtained using a VG Microscopes HB501UX scanning transmission electron microscope operating at 100-kV accelerating voltage with a probe size (fwhm intensity) of 2.2 Å, and they were recorded in 20-s scans directly onto Polaroid film.

High-T_c superconducting films

The high-T_c materials provide an ideal illustration of the intuitive imaging capabilities of the *Z*-contrast technique. Because they comprise a relatively complex unit cell, there are numerous possibilities for the location of a defect or interface within

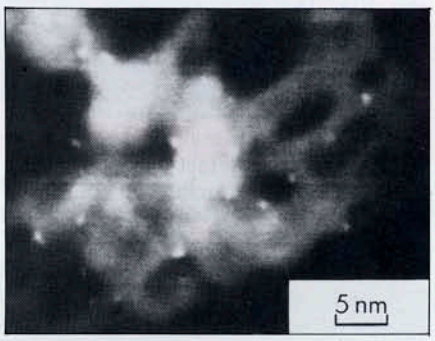

Figure 6. *Z*-contrast image of a 0.75% Pt catalyst on γ-alumina, showing 7–10-Å Pt clusters.
(Photograph courtesy of S. Bradley.)

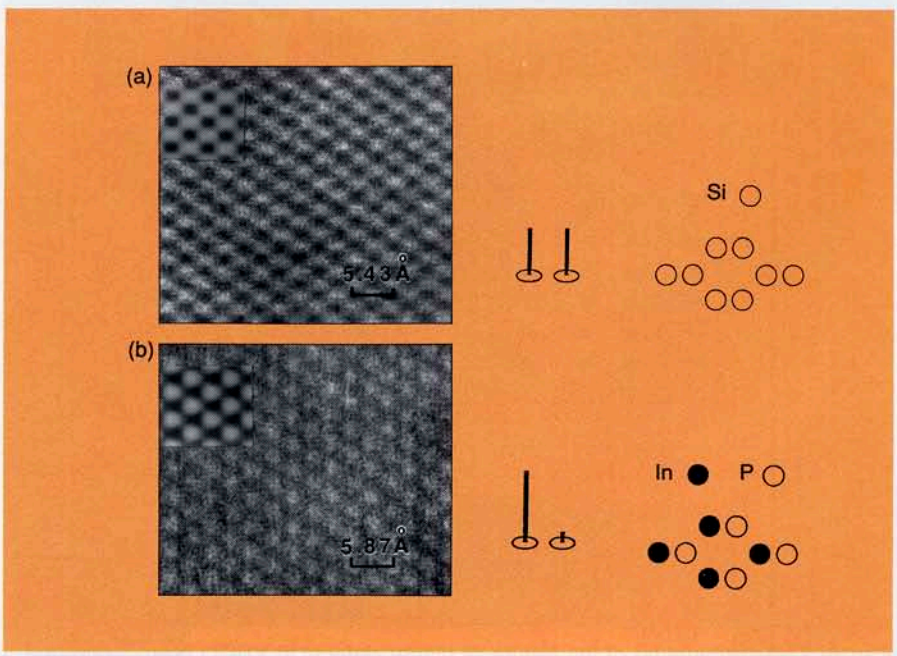

Figure 5. *Z*-contrast images of (a) Si and (b) InP.
Different shapes of image features correlate to the distribution of scattering power, indicated schematically by vertical lines.

the unit cell, each with its own structures. However, the insensitivity of the columnar s-states to their surroundings means that there are no proximity effects such as those that occur in conventional phase contrast imaging, and it is fairly easy to pick out the various atomic columns and identify the structure.

The *Z*-contrast images in Figure 7 show two kinds of planar defects commonly found in $YBa_2Cu_3O_{7-x}$ (YBCO) thin films (*13*). The brightest features in the image correspond to the Ba columns (Z = 56); the Y columns (Z = 39) appear significantly less bright. The Cu (Z = 29) are unresolved but contribute to the background in the image. Away from the defects, the tripled perovskite unit cell is quite apparent. It is also obvious that the planar defects are located between two adjacent Ba planes; the Ba columns adjacent to the defect show the same intensity as any other Ba column in the material. A simple measurement of the expansion across the defect indicates that there is extra material inserted, corresponding to an increase in separation of ~c/6. Because the defects appear dark, the extra material must be light, the most obvious candidate being Cu.

We can now understand the reason for the two different structures. An additional CuO plane must be shifted by half a unit cell along the a or b directions in the plane of the interface so that Cu in one sheet can bond to O in the other. In Figure 7a the shift is along the beam direction, whereas in Figure 7b it is perpendicular to the beam direction, resulting in the offset of the Ba columns. On close inspection, the Cu columns of the defects are just discernible, staggered in Figure 7b and merged into an elongated bridge in Figure 7a.

Cu-based defects are natural in these materials because they form the basis of the "247" and "248" phases. If impurity-based structures are likely, their presence could easily be checked by detecting the X-ray fluorescence generated by the electron beam. However, a larger beam—perhaps 1 nm in diameter located over the defects—would need to be used to obtain sufficient intensity.

Films grown at lower substrate temperatures show substantially more complicated defect structures and correspondingly degraded superconducting properties. Figure 8a shows an example of a film grown at 620 °C substrate temperature, with a very defective microstructure (*13*). Apart from the fact that the stoichiometry is close to that of the "247" phase, as evidenced by the extra CuO planes inserted between every alternate Ba plane, it is clear that the continuity of all planes has been broken. The central region, for example, shows a distinct shift by ~c/3 with respect to the upper and lower parts of the figure. These defects are clearly the reason for the poor superconducting properties; they originate from the substrate as a result of insufficient surface mobility at the low-growth temperatures.

A high growth temperature allows the film–substrate interface to rearrange its steps so that, one or two unit cells away, perfect continuity of the superconducting planes is achieved (Figure 8b), resulting in excellent transport properties. Through the *Z*-contrast images, we can see in a direct and simple manner how the superconducting properties correlate with the atomic-scale microstructure. From the nature of the defects, we also gain insight into the growth processes themselves—in this case, the importance of surface mobility. Connecting growth mechanisms to final film properties through the direct atomic-scale view of the microstructure is a key advantage of *Z*-contrast imaging.

The incoherent characteristics are of particular value in the study of interfaces; for example, they aid in understanding the role of grain boundaries in limiting the critical current capacity of a thin film and in understanding the characteristics of a tunnel junction. In both cases, we need to know the superconducting properties of the high-T_c material within a coherence length of the interface, which may be as small as 12 Å. Although the *Z*-contrast image is insensitive to oxygen, it can at least determine if the cation framework is correct and, if so, it might seem reasonable to assume that the structure could be oxygenated by a suitable processing treatment.

For a number of years, it has been difficult to understand the dramatic effect of a low-angle grain boundary in reducing a film's critical current

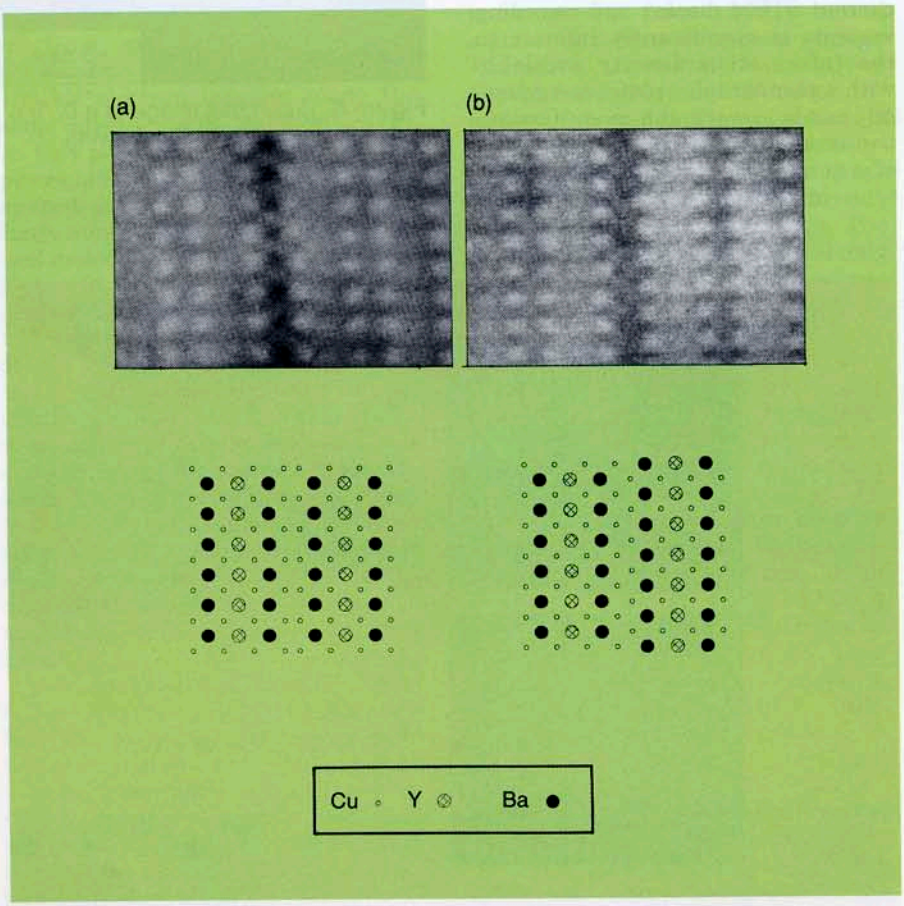

Figure 7. Determination of the nature of planar defects in YBCO from *Z*-contrast images.

The two *Z*-contrast images (a and b) correspond to the two possible projections shown. The light oxygen atoms contribute negligibly to the image and are omitted for clarity.

capacity. A low-angle grain boundary consists of an array of dislocations, and researchers generally have concluded that the dislocation cores must have induced impurity segregation or local nonstoichiometry, altering the superconducting properties. *Z*-contrast images have revealed, however, that compositional variations need not occur at such boundaries, which suggests an alternative explanation (*14*).

The dislocations comprising the boundary have an associated strain field extending over a significant range. Because quite a low strain (~1%) is sufficient to constrain the superconductor in its tetragonal phase, as grown, it seems very likely that each dislocation is surrounded by a substantial zone that can never transform to the orthorhombic superconducting phase, whatever the oxygen content. This simple model explains the critical current behavior. The superconducting properties of YBCO appear very sensitive to strain, and similar effects may well be found at interfaces in tunnel junctions and superlattices.

Recently it has been proved possible to map the chain site oxygen content of the superconductor on the nanometer scale. By passing the transmitted STEM beam through an energy loss spectrometer and observing the structure near the oxygen K shell absorption edge, the chain site oxygen atoms (representing x in $YBa_2Cu_3O_{7-x}$) can be resolved and quantified directly (*15*). A high-efficiency parallel detection system is required, however, to capture the data before this mobile oxygen becomes desorbed as a result of the high-energy electron beam.

Superconducting superlattices

There is much current interest in superlattices of YBCO with, for example, $PrBa_2Cu_3O_{7-x}$ (PBCO), an insulator of the same crystal structure. The interesting transport properties that result from changing the thickness of either layer type could provide considerable insight into the nature of superconductivity in these materials, provided that microstructural characterization can determine the morphology and compositional integrity of such structures.

Interdiffusion is a particular concern in the YBCO/PBCO system, because alloys of $Y_{1-y}Pr_yBa_2Cu_3O_{7-x}$ show a rapid reduction of T_c with increasing Pr content; they eventually become semiconducting at $y \geq 0.5$ (*16*). The general trend in the superlattice case is that T_c decreases both

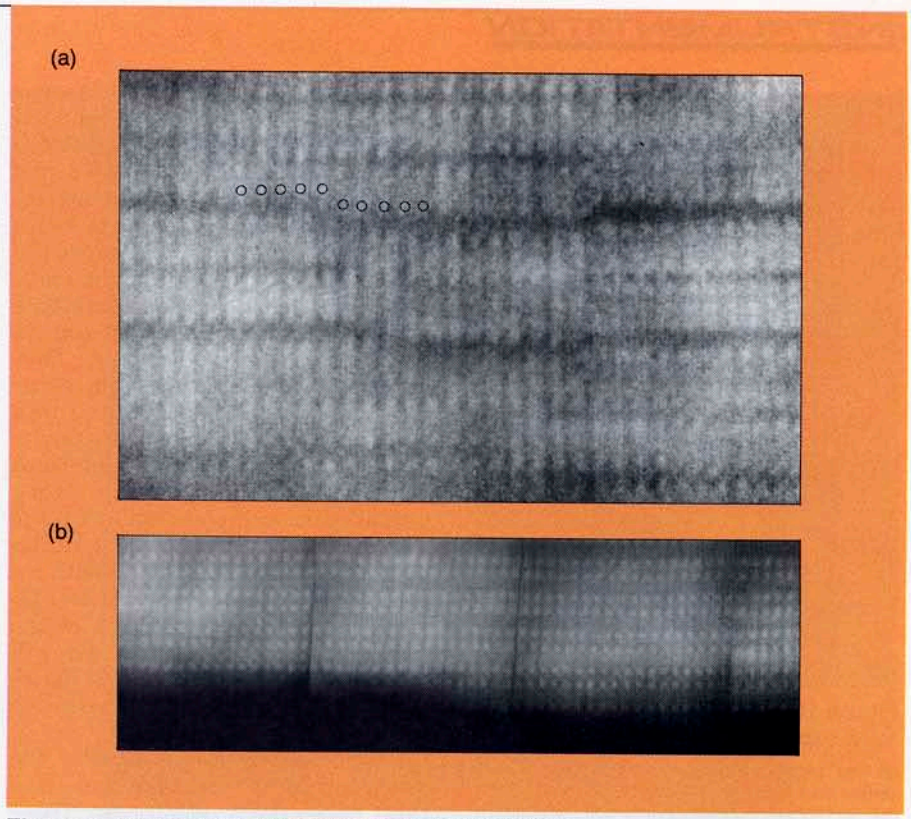

Figure 8. *Z*-contrast images of superconductor films.

(a) Disrupted planes resulting from reduced substrate temperature during deposition (620 °C). (b) Perfect crystallinity achieved at high temperatures (670 °C).

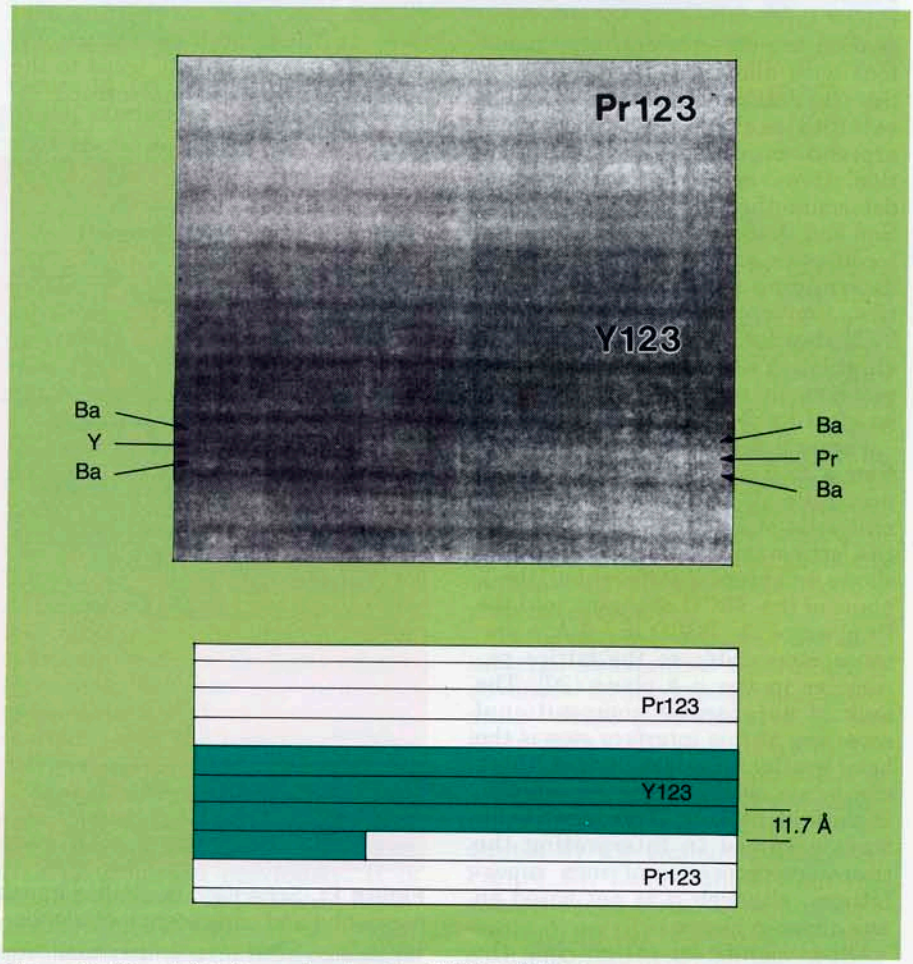

Figure 9. Abrupt interface step in a 3 × 5 YBCO/PBCO superlattice.

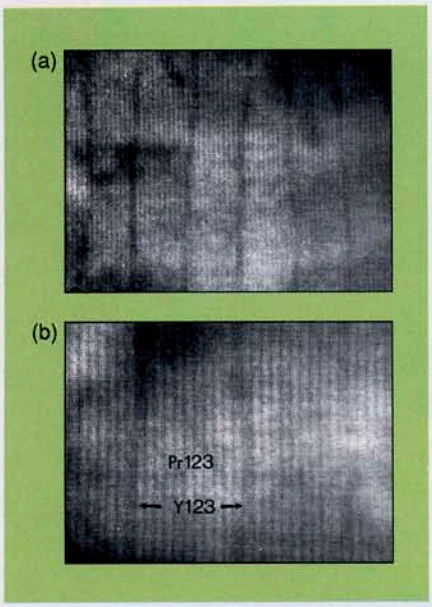

Figure 10. *Z*-contrast images of a 1×8 superlattice.

(a) Low magnification showing YBCO cells as vertical dark lines jumping repeatedly by one unit cell. (b) Higher magnification showing individual planes.

as the thickness of the YBCO layer decreases and as the thickness of the PBCO layer increases (*17–19*). This general trend seems entirely consistent with alloy formation, although the observation of X-ray diffraction satellite peaks does indicate the presence of a superlattice modulation. However, it cannot accurately determine the depth of that modulation and therefore cannot exclude interdiffusion as a significant factor in determining the transport properties. Conventional high-resolution TEM thus far has been unable to distinguish YBCO from PBCO; the problem, therefore, would appear to be ideal for *Z*-contrast investigation.

Figure 9 shows a *Z*-contrast image from a 3×5 superlattice (nominally 3 unit cells of YBCO separated by 5 unit cells of PBCO). As indicated in the schematic, this image clearly shows an abrupt interface step, the Y plane of the YBCO changing into the Pr plane of the PBCO in ~4 Å, a distance comparable to the lattice parameter in the *a–b* plane (*20*). The lack of substantial compositional smearing at this interface step is the best available evidence that there can be no substantial interdiffusion in these structures. (This result is always assumed in interpreting the transport properties of such superlattices, although it is not based on any direct evidence.)

Other significant insight into the growth mechanism can be obtained by realizing that the YBCO layer is in fact acting as a marker, replicating the surface of the growing PBCO at the time the laser ablation target was switched. The superlattice, therefore, provides a series of snapshots showing the evolution of the film morphology on the atomic scale. Figure 10 shows a 1×8 superlattice in which the individual unit cells of YBCO are clearly delineated. They are continuous, apart from occasional jumps by one structural unit cell. This is a clear demonstration of cell-by-cell growth; the single unit cell of YBCO shows a very strong tendency to complete its coverage before a new layer of PBCO is nucleated. It is in complete accord with recent observations of RHEED oscillations having the periodicity of the *c*-axis lattice parameter (*21*). Growth is occurring via the sequential nucleation and coalescence of islands 11.8 Å in height.

When the layer is complete, the surface supersaturation increases until nucleation events occur. These new islands then grow, reducing the surface supersaturation, until they coalesce and the cycle repeats. This statistical growth process leads to a gradual roughening of the film surface, as illustrated in Figure 11, which in turn gradually leads to the buildup of the more macroscopic islands that have been observed by STM (*22*).

The intrinsic island size during the highly nonequilibrium growth conditions is on the order of the separation of the unit cell jumps in the YBCO, typically 20–30 nm (see Figure 10). The sharp interface step seen in Figure 9 also implies that the edge of the island is parallel to the ⟨100⟩ electron beam direction for the entire thickness of the specimen, which is estimated at 10–20 nm. Although we do not have sufficient surface mobility for step flow growth, which would produce atomically smooth surfaces (Figure 11), the mobility is still sufficient for the islands to grow and coalesce perfectly, avoiding the *c*/3 defects seen at lower growth temperatures (Figure 8a).

The only remaining question is which plane terminates the growing surface. If we look at an amorphous–crystal interface produced by ion implantation, we realize that at the end of the ion range amorphization is essentially the time-reversed process of growth. In Figure 12, we see that amorphization has also occurred, remarkably, cell by cell, and that the interface is located at the Cu-chain plane (*20*). The basic building block of high-T_c films, for growth and amorphization, is therefore the Ba–Y–Ba (or Ba–Pr–Ba) structural unit.

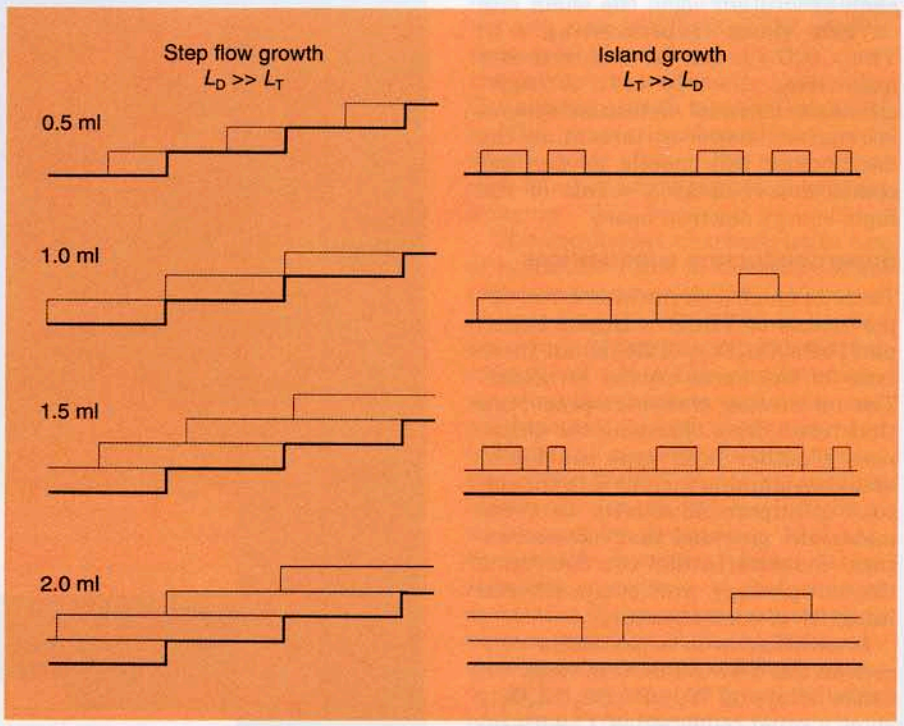

Figure 11. Schematic illustrating transition from step flow growth to sequential nucleation and coalescence of islands.

The transition occurs as the surface diffusion length L_D becomes less than the terrace length L_T, and results in roughening of the surface morphology. The term ml refers to monolayer.

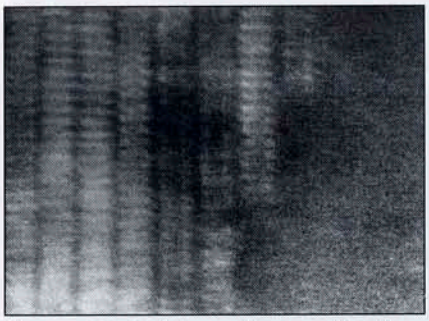

Figure 12. Cell-by-cell amorphization of YBCO via oxygen ion implantation; amorphous interface is located at the Cu-chain plane and jumps repeatedly by one unit cell.

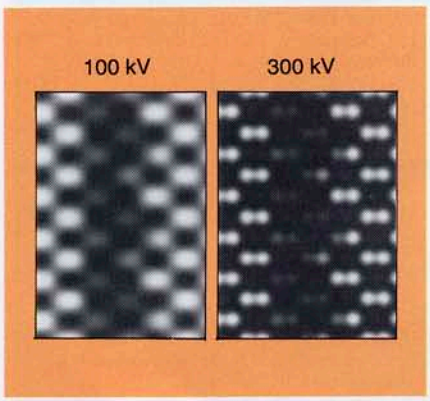

Figure 13. Simulated *Z*-contrast images of interfacial ordering in a $(Si_4Ge_8)_n$ superlattice for 100-kV and 300-kV microscopes.

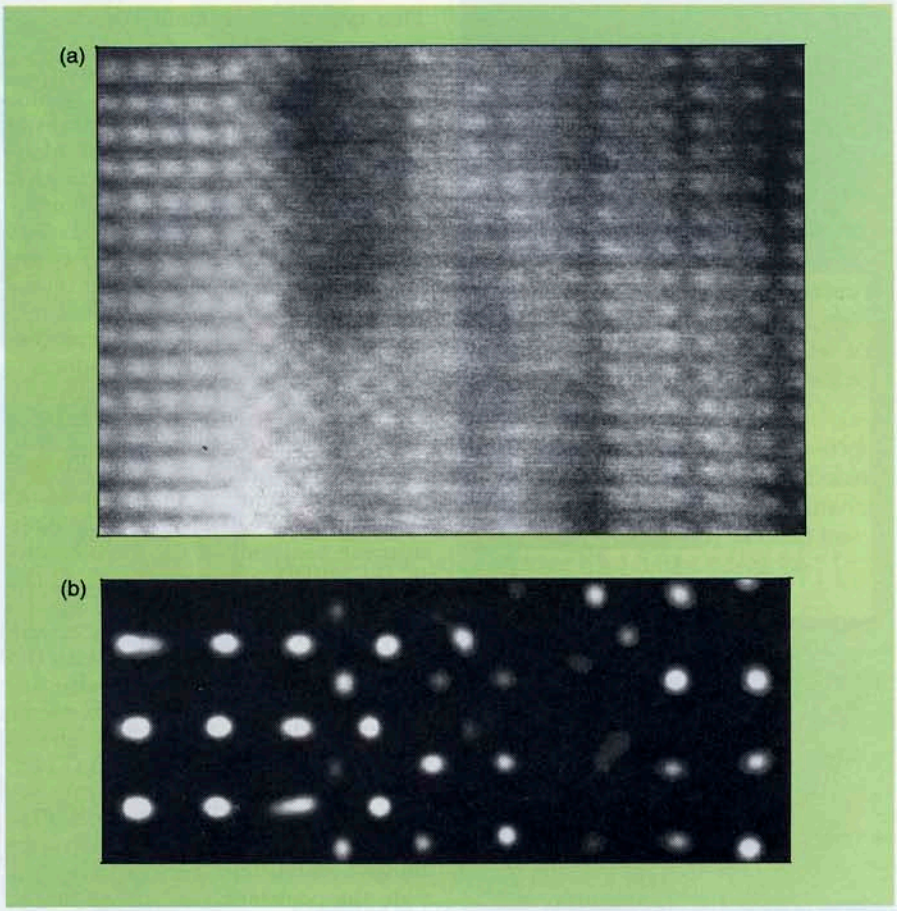

Figure 14. (a) Image and (b) maximum entropy reconstruction from a YBCO–$KTaO_3$ interface.

(Reconstruction courtesy of T. Ferridge using Cambridge MemSys 5 software of J. Skilling and S. F. Gull.)

This result, of course, is quite consistent with the known chemistry of the system; growth occurs in the tetragonal phase regime when there are few oxygen atoms in the CuO plane, and bonding across this plane is expected to be weak. This property does, however, result in the remarkable structural stability of the large Ba–Y–Ba block, which in turn ensures that growth can occur free from structural defects.

One question that naturally arises out of this microscopic view concerns the effect of the jumps or interface steps on the transport properties. In the $1 \times N$ superlattices, there is obviously very little overlap between two adjacent islands that are displaced vertically by one unit cell. In a sense, the current is forced to travel along the c axis for a small distance, and it seems likely that this would result in substantially reduced critical currents. For a $2 \times N$ superlattice, the region of overlap would be increased to one island diameter on average, and excellent "film-like" critical current behavior has been obtained (*20*). Even though the individual YBCO layers are quite wavy, the current can follow these modulations with no deleterious effects. This is an important advantage of YBCO materials over Bi- or Tl-based compounds, which are much more two-dimensional in their superconducting properties.

Discussion

It is hoped that this detailed discussion of the high-T_c superlattices has illustrated how direct imaging by *Z*-contrast STEM can provide insight into a materials problem. This kind of insight provides the long-sought-after link between the measured properties, the atomic-scale microstructure, and the growth processes that created it.

We can now see interface structures directly; often the actual structures present have never been seen or even proposed previously. It is natural to choose the simplest interface structure to match to one's data, but there is no guarantee that nature will do likewise. It is the ability to go from the image back to the object that is the most exciting aspect of *Z*-contrast imaging. The structures we deduce, and the atomic-scale growth processes suggested by them, provide ideal input for theoretical modeling of interface properties and growth mechanisms. Theory cannot at present predict the behavior of an interface without some guide as to the actual structure. It can, however, rationalize what we see, adding to the depth of understanding about the atomic-scale processes that control materials properties.

The *Z*-contrast technique will soon undergo substantial instrumental advances. By increasing the accelerating voltage from the existing 100 kV to 300 kV, the resolution will correspondingly decrease from 2.2 Å to a predicted 1.4 Å. Our view of materials will clarify tremendously, as indicated by the simulated images in Figure 13. Each dumbbell in the semiconductor structure will become resolved, greatly improving the compositional sensitivity for the pairs of columns comprising the dumbbells.

This type of instrument currently is being constructed.

Furthermore, the incoherent nature of the image means that resolution enhancement can be achieved through a suitable computer algorithm to remove or reduce the instrumental broadening. It is a fundamental advantage of the *Z*-contrast approach that the high-frequency information is contained in the image through the shapes of image features (see Figure 5). How this information can be extracted by a maximum entropy reconstruction is illustrated in Figure 14 for the case of an interface between a YBCO film and a $KTaO_3$ substrate. Tracing across from the bright Ta columns in the substrate in Figure 14a, we find that they fade into the positions of the Cu columns in the YBCO, whereas the K of the substrate (not directly visible) turns into the bright Ba columns of the YBCO. This is all consistent with the various ionic sizes, but it is also apparent from the image that for one or two unit cells a compound is formed that appears to project as $BaTaO_3$, which is not stable in bulk form.

The maximum entropy result (Figure 14b) shows substantially enhanced resolution and can also provide the positions and intensities of the various columns with associated individual error bars. It provides an ideal way to quantify the image. Combined with the higher accelerating voltage, it will allow quantitative information to be extracted from *Z*-contrast images to a scale even below 1 Å.

Truly, it is an exciting time to be involved in materials research.

All research described here was performed in collaboration with my colleagues D. E. Jesson, M. F. Chisholm, O. W. Holland, D. H. Lowndes, D. P. Norton, R. Feenstra, and S. Bradley, and was sponsored by the Division of Materials Sciences, U.S. Department of Energy, under contract DE-AC05-84OR21400 with Martin Marietta Energy Systems, Inc.

References

(1) See, for example, Cowley, J. M. In *High-Resolution Transmission Electron Microscopy*; Buseck, P.; Cowley, J.; Eyring, L., Eds.; Oxford University Press: New York, 1988; Chapters 1–2, pp. 3–57.
(2) For an elementary introduction, see Pennycook, S. J. *Contemp. Phys.* **1982**, *23*, 371.
(3) Brown, L. M. *J. Phys.* **1981**, *F11*, 1.
(4) Colliex, C.; Mory, C. In *Quantitative Electron Microscopy*; Chapman, J. N.; Craven, A. J., Eds.; Scottish Universities Summer School in Physics: Edinburgh, Scotland, 1984; Chapter 5, pp. 149–216.
(5) Pennycook, S. J.; Jesson, D. E. *Phys. Rev. Lett.* **1990**, *64*, 938.
(6) Howie, A. *J. Microsc.* **1979**, *117*, 11.
(7) Jesson, D. E.; Pennycook, S. J.; Baribeau, J-M. In *High Resolution Electron Microscopy of Defects in Materials*; Sinclair, R.; Smith, D. J.; Dahmen, U., Eds.; Materials Research Society: Pittsburgh, PA, 1990; p. 223.
(8) Pennycook, S. J.; Jesson, D. E.; Chisholm, M. F. *Proc. SPIE Int. Soc. Opt. Eng.* **1990**, *182*, 1284.
(9) Jesson, D. E.; Pennycook, S. J.; Baribeau, J-M. *Phys. Rev. Lett.* **1991**, *66*, 750.
(10) Treacy, M.M.J.; Rice, S. B. *J. Microsc.* **1989**, *156*, 211.
(11) Pan, M.; Cowley, J. M.; Chan, I. Y. *Ultramicroscopy* **1990**, *34*, 93.
(12) Rice, S. B.; Koo, J. Y.; Disko, M. M.; Treacy, M.M.J. *Ultramicroscopy* **1990**, *34*, 108.
(13) Pennycook, S. J. et al. *Mater. Res. Soc. Symp. Proc.* **1990**, 169.
(14) Chisholm, M. F.; Pennycook, S. J. *Nature* **1991**, *351*, 47.
(15) Browning, N. D.; Brown, L. M. *Supercond. Sci. Technol.* **1991**, *4*, 5346.
(16) Peng, J. L. et al. *Phys. Rev. B* **1989**, *40*, 4517.
(17) Triscone, J-M. et al. *Phys. Rev. Lett.* **1990**, *64*, 804.
(18) Li, Q. et al. *Phys. Rev. Lett.* **1990**, *64*, 3086.
(19) Lowndes, D. H.; Norton, D. P.; Budai, J. D. *Phys. Rev. Lett.* **1990**, *65*, 1160.
(20) Pennycook, S. J. et al. *Phys. Rev. Lett.* **1991**, *67*, 765.
(21) Terashima, T. et al. *Phys. Rev. Lett.* **1990**, *65*, 2684.
(22) Schlom, D. G. et al., submitted for publication in *Z. Phys. B.*

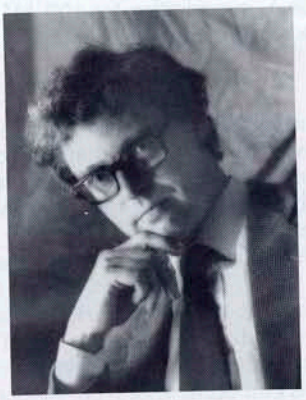

S. J. Pennycook is a senior research scientist in the Solid State Division at ORNL and leader of the electron microscopy group. He obtained his Ph.D. in physics from the University of Cambridge (England) in 1978 and moved to Oak Ridge in 1982. His main research interests are the study of artificially structured and modified semiconductors and superconductors through the technique of Z-contrast STEM. The development of this technique earned Pennycook the 1989 Department of Energy award for outstanding scientific accomplishment and an R&D 100 award in 1990. He is a fellow of the American Physical Society and a member of the Materials Research Society and the Electron Microscopy Society of America.